Research Article | Vol. 33, No. 8 / 21 Apr 2025 / Optics Express 17002
Optics EXPRESS

Liquid and gas mid-infrared integrated spectroscopic sensor

SOFIANE MEZIANI,[1] ABDELALI HAMMOUTI,[1] ABDALLAH JAAFAR,[1] LOÏC BODIOU,[1] NATHALIE LORRAIN,[1] PARASTESH PIRASTEH,[1] RADWAN CHAHAL,[2] ALBANE BÉNARDAIS,[2] RÉMI COURSON,[3] JOHANN TROLES,[2] CATHERINE BOUSSARD-PLEDEL,[2] VIRGINIE NAZABAL,[2] MOHAMMED GUENDOUZ,[1] AND JOËL CHARRIER[1,*]

[1] *Univ Rennes, CNRS, Institut Foton-UMR 6082, 22305 Lannion, France*
[2] *CNRS UMR 6226 ISCR, Université de Rennes, 22302 Rennes, France*
[3] *Ifremer, RDT Research and Technological Development, F-29280 Plouzané, France*
[*] *joel.charrier@univ-rennes.fr*

Abstract: Mid-infrared (mid-IR) waveguide sensors were fabricated using two platforms: chalcogenide glasses (ChGs) and porous silicon (PSi). ChGs layers were deposited through RF magnetron sputtering while PSi layers were prepared by electrochemical anodization. Ridge waveguides were patterned using standard i-line photolithography and reactive ion etching for both platforms. The ChGs waveguides exhibit a wide transparency range from $\lambda = 3.94$ to 8.95 µm, with a minimum propagation losses value of 2.5 dB/cm at $\lambda = 7.58$ µm, while PSi transparency range is from $\lambda = 3.94$ to 4.55 µm with a minimum propagation losses value of 9.1 dB/cm at $\lambda = 4.12$ µm. To validate the proposed ChGs sensor, a spectroscopic liquid sensing experiment was performed using acetonitrile and isopropanol. The results showed an estimated limit of detection (LoD) of 610 ppm at $\lambda = 4.44$ µm for acetonitrile and a LoD of 300 ppm at $\lambda = 7.25$ µm for isopropanol, enabled by the evanescent field interaction. Regarding gas sensing, CO_2 was used as the analyte. A LoD of 17000 ppm at $\lambda = 4.28$ µm was achieved using the ChGs platform. The sensing application was improved with the PSi platform. Due to the open pores, light and gas molecules interact within the internal volume, unlike the ChGs platform, where the interaction occurs with the evanescent part of the light. This results in an exalted external confinement factor, Γ, over 75 times greater for the PSi platform, achieving a LoD of 600 ppm at $\lambda = 4.26$ µm for CO_2 sensing. Estimation of concentrations from mixtures of two solutions through deconvolution of the measured spectra was also achieved with good approximations, validating the transduction capabilities in a complex environment using the ChGs platform.

1. Introduction

In recent years, there has been an increasing scientific focus on developing mid-IR photonic circuits specifically for optical sensing applications [1]. This interest has grown significantly due to remarkable advancements in optical sources like quantum cascade lasers (QCLs) [2], Interband cascade lasers (ICLs) [3] and supercontinuum sources [4]. The mid-IR wavelength range corresponds to the absorption bands of many toxic and pollutant molecules [5], making mid-IR spectroscopic sensors highly suitable for a wide variety of in-situ and challenging environmental applications. This level of performance has created an innovative need for materials and guiding structures. The use of integrated optical circuits as sensors presents several benefits, including lower manufacturing costs and more compact packaging, allowing for efficient

#553730 https://doi.org/10.1364/OE.553730
Journal © 2025 Received 20 Dec 2024; revised 15 Mar 2025; accepted 19 Mar 2025; published 9 Apr 2025

Optics EXPRESS

on-site measurement. However, the fabrication of these circuits requires the use of materials that are transparent in the mid-IR spectrum. Chalcogenide glasses (ChGs) and porous silicon (PSi) show great potential for the design of such circuits [6–9].

ChGs display a wide transparency window stretching from near-infrared into the mid-IR, up to 11 µm for sulfides, 15 µm for selenides, and 20 µm for tellurides [10]. They offer a range of advantageous properties for optical applications. Their refractive index can be precisely tuned by altering their composition, enabling accurate and efficient shaping of guiding structure. Furthermore, their high non-linear refractive index facilitates the occurrence of efficient non-linear phenomena, requiring lower incident powers or shorter lengths of light-matter interaction compared to silica and fluoride glasses [11,12]. Their low phonon energies also make them ideal hosts for rare-earth dopants [13]. ChGs have proven to be suitable for broadband mid-IR supercontinuum applications [14]. The potential of ChGs for designing guiding structures in integrated optics has been demonstrated in multiple studies. Propagation losses of 0.6 dB/cm were reported at wavelengths between $\lambda = 2.5$ and 3.7 µm [15], and high-quality factor ring resonators have been achieved at $\lambda = 5.2$ µm [16]. Advancements in the fabrication of ChG structures have led to a variety of sensing applications based on evanescent field spectroscopy. A rib $Ge_{11.5}As_{24}Se_{64.5}$ waveguide was used for sensing, as demonstrated with a solution of Prussian blue in Dimethyl Sulphoxide [17]. A methane gas sensor was demonstrated using a $Ge_{28}Sb_{12}Se_{60}$ waveguide [18]. Other sensing demonstrations were reported using ChGs for Isopropanol [19], SF_6 [20] and CO_2 [21].

Regarding porous silicon, it is transparent up to 8 µm and offers a porous structure, meaning it possesses pores and silicon crystallites at the nanoscale. The volume fraction of air corresponds to the porosity of the porous layer. This porosity can be modulated based on the parameters of anodization and is directly related to the refractive index. As porosity increases, the refractive index approaches that of air. The successive fabrication of multiple porous layers with different refractive indices allows for the creation of various optical structures such as waveguides [22], microresonators [23], Bragg mirrors [24], and microcavities [25]. In addition to its compatibility with CMOS technology [26], porous silicon holds great potential for the design of integrated optical circuits in the mid-IR domain [27]. Optical multilayer Bragg reflectors have been implemented using PSi layers in the Mid-IR [28].

The advantage of having a porous layer lies in the fact that the pores allow the penetration of substances in gaseous or liquid form into the integrated optical circuit. This increases the interaction between the probed molecules and the guided optical mode [29]. Consequently, this interaction within the internal volume [30]. This provides a large specific surface area, which can reach up to 800 m2cm-3 [31], making it also useful as a sacrificial layer in surface micromachining [32,33]. Additionally, these porous layers can be infiltrated with a variety of media, such as liquid crystals, thus offering the possibility of modifying photonic band gaps [34,35].

The sensing application of PSi has already been demonstrated in several publications, including the detection of various molecules in the gas phase [36,37] and liquid phase [38], humidity levels [39,40] and alcohol concentration [41]. It has also been used for the immobilization of DNA strands [42–44], detection of proteins and enzymes [45,46], hydrocarbons [47] and the detection of explosive vapors after surface functionalization with polymers [48]. In this paper, we compare mid-infrared ChGs and PSi platforms for CO_2 sensing. The PSi platform, with its porous structure, enhances light-matter interaction, overcoming the sensitivity limits of bulk materials, albeit with higher propagation losses and a shorter wavelength transparency range. By contrast, the ChGs platform exhibited lower sensitivity for CO_2 sensing. However, it leverages its broad transparency window to enable, in addition to gas-phase CO_2 detection, the sensing of liquid-phase analytes, such as acetonitrile and isopropanol with lower propagation losses. To address the challenge of sensing in complex environments, this work experimentally demonstrates the capabilities of the

Optics EXPRESS

ChGs platform by quantifying the relative concentrations of isomers 1-propanol and 2-propanol in mixed liquid solutions. These results highlight the potential of the developed platforms for real-world applications requiring multiphase detection and environmental analysis of various molecules. Figure 1 illustrates the waveguide transducer configuration used for both platforms. To control light-matter interaction within the ridge waveguide during sensing measurements, a polydimethylsiloxane (PDMS) microfluidic channel was bonded to the sample.

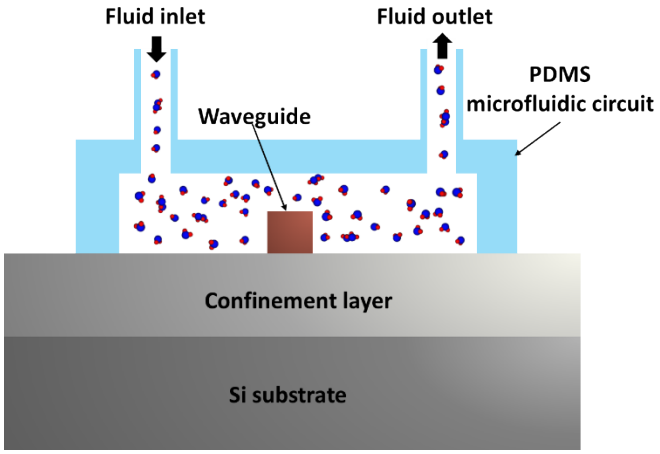

Fig. 1. Schematic of the waveguide transducer configuration used for both platforms. In the ChGs platform, the guiding and confinement layers are composed of $Ge_{12.5}Sb_{25}Se_{62.5}$ and $Ge_{28.1}Sb_{6.3}Se_{65.6}$ respectively. In the PSi platform, the guiding and confinement layers consist of porous silicon with 60% and 73% porosity, respectively

2. Materials and methods

To support single-mode light propagation, the ridge waveguide structures were designed using a commercial software (FIMMWAVE, Photon Design), which also provided the external confinement factor Γ, a parameter that evaluates the fraction of the electric field interacting with the target analyte [49]. Γ is defined as below:

$$\Gamma = \frac{n_g}{n_{superstrat}} \frac{\iint_{superstrate} \varepsilon |\vec{E}|^2 \mathrm{d}x\mathrm{d}y}{\iint_{\infty} \varepsilon |\vec{E}|^2 \mathrm{d}x\mathrm{d}y} \tag{1}$$

With n_g the group index, $n_{superstrate}$ the refractive index of the active sensing area, ε the permittivity and $\vec{E}$ the electric field.

In the case of waveguide based on porous material, light and molecules interact in the inside volume due to the open pores. From Eq. (1) the value of Γ can be expressed as follows:

$$\Gamma = n_g \left(\frac{S_{air} + \varepsilon_{guide} S_{guide} Porosity_{guide} + \varepsilon_{clad} S_{clad} Porosity_{clad}}{S_{air} + \varepsilon_{guide} S_{guide} + \varepsilon_{clad} S_{clad}} \right) \tag{2}$$

With ε_{guide} and ε_{clad} representing the permittivity in the guide and cladding layer, respectively, S_{air}, S_{guide} and S_{Clad} are the integrals of the square of the field in the air, guiding, and cladding regions, respectively.

The ChGs samples were fabricated with a confinement layer of $Ge_{28.1}Sb_{6.3}Se_{65.6}$ with a thickness of 5 μm, and a guiding layer of composition $Ge_{12.5}Sb_{25}Se_{62.5}$. The layers were grown

Optics EXPRESS

on an n-type Si substrate using RF magnetron sputtering [9]. The refractive index values for the guiding and confinement layers were 2.77 and 2.49, respectively. These values remained relatively constant across the working wavelength range of λ = 3.94 to 8.95 µm.

For the PSi sample, the guiding and cladding layers were fabricated using a heavily doped P-type silicon (100) substrate with a resistivity of 5 mΩ.cm. The layers were formed by applying current densities of 50 mA/cm^2 and 100 mA/cm^2 for durations of 65 seconds and 102 seconds, respectively. The electrolyte consisted of hydrofluoric acid, ethanol, and deionized water in a 2:2:1 ratio. The refractive index was adjusted by varying the porosity, which was controlled by the applied current density [50]. As a result, two layers were produced: a 2.2 µm guiding layer with 60% porosity and a refractive index of 1.71, and a 5 µm cladding layer with 73% porosity and a refractive index of 1.48, both measured at a wavelength of 4.28 µm. The refractive index of each PSi layer was determined using FTIR reflectance spectra, with experimental spectral fringes fitted according to the Bruggeman effective medium approximation theory [51].

Following the fabrication of the thin film layers for both platforms, ChGs ans PSi, single mode ridge waveguides were fabricated using a conventional i-line photolithographic process. This was followed by a dry etching procedure. For ChGs platform, the etching process utilized a gas mixture of 5 sccm CHF_3 at a pressure of 5 mTorr, with an ICP power of 75 W and an RF power of 25 W. Regarding the PSi platform, the waveguide was obtained through a dry etching step using 20 sccm of CHF_3 at a pressure of 5 mTorr, with an ICP power of 400 W and an RIE power of 25 W.

It should be noted that the dimensions of the waveguides are specifically designed for the respective operating wavelengths, in order to achieve single-mode propagation . At λ = 4.28 µm, the thickness of the ChGs guiding layer was h = 1.2 µm, and the width of the waveguide was w = 6 µm this sample is noted "sample A" (Fig. 2(a)). For sensing measurements at a wavelength of 7.25 µm, the thickness of the ChGs guiding layer was increased to h = 1.9 µm, and the width of the waveguide was w = 8 µm. This sample is referred to as "Sample B". PSi sample destinated for CO_2 sensing is labeled "Sample C" (Fig. 2(b))., featuring a guiding layer thickness of h = 2.2 µm and a waveguide width of w = 6 µm. Table 1 summarizes the characteristics of the fabricated samples, including the corresponding external confinement factors.

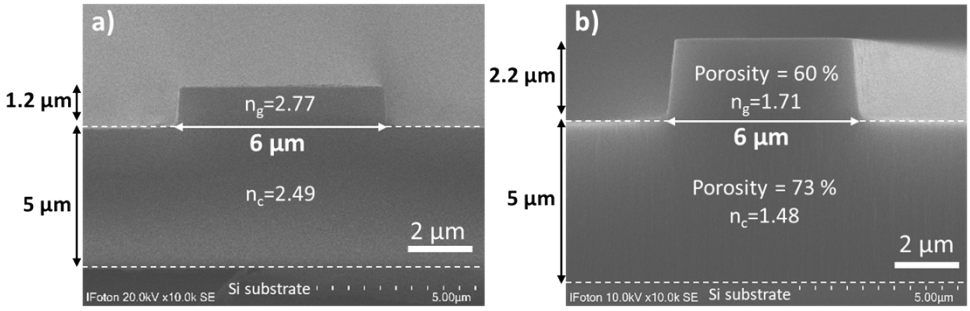

Fig. 2. SEM Image of fabricated ridge waveguide using platform form a) ChGs b) PSi

2.1. *Mid-infrared optical bench and propagation losses*

A mid-IR optical bench setup was assembled for the optical characterization of the guiding structures, as shown in Fig. 3. A tunable QCL source (*MIRCAT, Daylight Solutions*) was used, with an operating wavelength rang from λ = 3.94 to 4.6 µm and λ= 6.9 to 11 µm. Butt coupling method was used between ChGs fiber and waveguides. At the output, the light beam from the waveguide was collimated into a detector using a ZnSe objective lens. Two detectors were used for the acquisition depending on the wavelength range: the *DSS-PSE020 T, Horiba* for 3.9 - 4.6

Optics EXPRESS

Table 1. Dimensions of waveguides used for operating wavelength ranges

Name	Sample A	Sample B	Sample C
Platform	ChGs	ChGs	PSi
Wavelength range (μm)	3.94–4.6	6.9–8.95	3.94–4.55
Thikness (μm)	1.2	1.9	2.2
Width (μm)	6	8	6
Γ_{TE}	9.1% (*at* λ= 4.28 μm)	5% (*at* λ= 7.25 μm)	111% (*at* λ= 4.26 μm)
Γ_{TM}	1.4% (*at* λ= 4.28 μm)	1.4% (*at* λ= 7.25 μm)	115% (*at* λ= 4.26 μm)
Sensing experiment	CO_2 and Acetonitrile	Isopropanol	CO_2

μm and the nitrogen-cooled *DSS-MTC(14)-020 L, Horiba* for 6.9 - 9 μm. The photolithography mask used in the fabrication included several sets of waveguides with varying lengths, allowing for the measurement of propagation losses using a non-destructive cut-back method. The QCL emission is polarized perpendicular to the base of the laser. However, since the fiber affects the mode's polarization, the coupled mode in the ridge waveguide is a random combination of the two fundamental modes. To properly perform the optical characterizations, the chalcogenide glass fiber's position must remain fixed throughout the measurements to maintain a stable coupling mode.

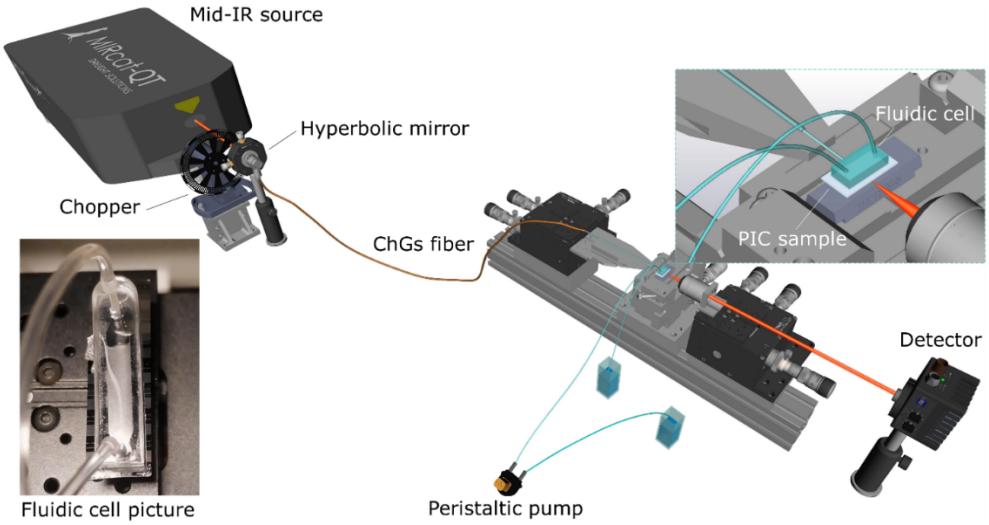

Fig. 3. Schematic diagram of the optical bench platform sensor

To control the light-matter interaction within the ridge waveguide during the sensing test, a *PDMS* cell with a microchannel (500 μm thick, 5 mm wide, and 28 mm long) was bonded to the sample using O_2 plasma treatment.

The transmission of the waveguides was measured for each sample using the optical characterization bench. Sample A was used with waveguide lengths ranging from 10 to 15 mm, in 0.5 mm increments, over the wavelength range of λ = 3.9 to 4.6 μm. For sample B, the waveguide lengths ranged from 10.6 to 15.6 mm, also incremented by 0.5 mm, and measurements were performed in the wavelength range of λ = 7 to 8.95 μm. Sample C was used with waveguide lengths varying from 6.3 to 17.3 mm, with increments of 2 mm (except for the first increment of

Optics EXPRESS

1 mm). A decreasing exponential function was fitted to the measured signals to determine the propagation loss, for each wavelength range measurement.

Since no specific analyte is targeted during the propagation loss measurements, the contribution of absorption in the Beer-Lambert law is negligible. The behaviour of the transmitted signal can be described as follows:

$$P(\lambda) = P_0(\lambda)\, e^{-\alpha(\lambda)\, L_{waveguide}} \tag{3}$$

where P_0 is the input optical power, α are the propagation losses, and $L_{waveguide}$ is the length of the waveguide.

Figure 4 compares the propagation losses between ChGs and PSi. From $\lambda = 4$ to 4.2 µm, ChGs show lower propagation losses with Sample A, exhibiting values around 5.5 dB/cm, compared to PSi with Sample C, which exhibits higher values around 10 dB/cm. The absorption peak corresponding Se-H bond [52] in ChGs sample is visible on the propagation losses curve around $\lambda = 4.6$ µm, increasing losses up to 16 dB/cm. The drastic increase in loss values measured with the PSi sample is primarily attributed to free carrier absorption in the heavily doped bulk silicon substrate [53], scattering [54], and the adsorption of various molecules from ambient air within the pores. Additionally, silica (SiO_2) forms on the sample's surface due to interaction with ambient air, and its absorption in the working wavelength range further increases the propagation losses [30]. Recent work using slot waveguides [55], which enable volume interaction with the analyte, reported similar propagation losses of 10.4 dB/cm at $\lambda = 3.27$ µm. The contribution of adsorption losses from molecules present in the air was demonstrated by repeating the propagation loss measurements under nitrogen flow, which reduced the losses to 8.3 dB/cm.

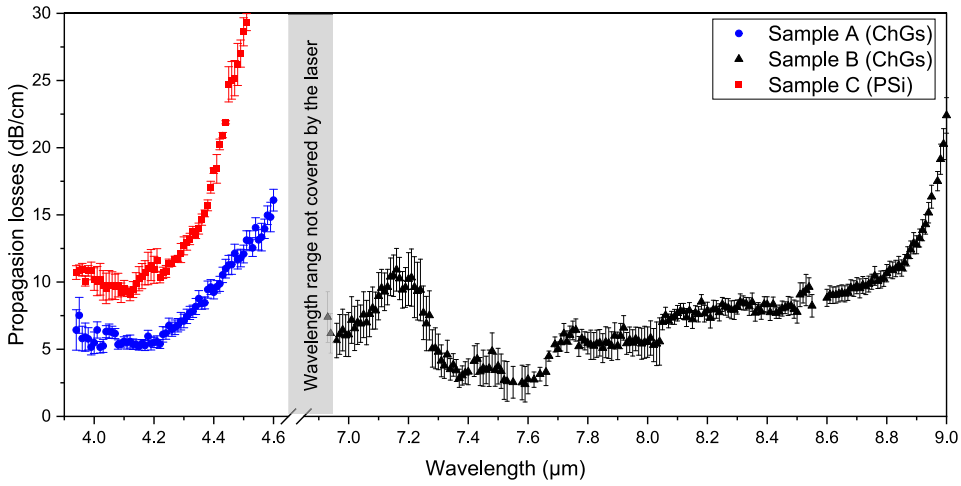

Fig. 4. Propagation losses as a function of wavelength for ChGs and PSi ridge waveguides.

Propagation losses in higher wavelength range are achieved with sample B on the ChGs platform. An average propagation losses value of 6.5 dB/cm are obtained from $\lambda = 7$ to 8.6 µm. The losses increase beyond 8.6 µm due to the waveguide dimensions not being optimized for these higher wavelengths. It can be observed that the minimum loss value of 2.5 dB/cm is obtained at $\lambda = 7.58$ µm, which aligns with the values reported in the state of the art for this wavelength range [56–59].

Propagation loss values are closely linked to the roughness of the waveguide sidewalls. Since the propagation is monomodal, the optical mode interacts strongly with the waveguide and substrate surfaces, where high roughness can lead to significant losses. Additionally, chemical residues, particularly fluoropolymers from the dry etching process, can absorb light at the working

Optics EXPRESS

wavelength, further increasing losses. These fluoropolymers deposit on the guiding structures during the dry etching process in the cleanroom. The influence of fluoropolymers on the ChGs platform was demonstrated by Ma et al. [60].

3. Sensing demonstration

Sensing tests were conducted on both platforms: using CO_2 for the PSi and using CO_2, acetonitrile, and isopropanol for the ChGs. The use of the PSi platform was limited to CO_2 due to its short transparency range, which does not cover the absorption peaks of acetonitrile and isopropanol.

3.1. Liquid sensing tests

For liquids analytes, we present the sensing tests performed using the ChGs platform. For wavelengths around 4 µm, nitriles are characterized by a sharp and high-intensity absorption band, corresponding to the C≡N stretching vibration between 4.42 and 4.5 µm [62]. We specifically chose acetonitrile due to its prominent absorption peak at 4.44 µm as shown in Fig.4a [63,64]. Isopropanol was also used due to its characteristic ν(C-C) stretching vibrational mode at 7.25 µm [65] as shown in Fig. 4(b). A peristaltic pump was used to control the flow of analytes through the fluidic cell at a rate of 300 µL.min^{-1}. To prepare the different concentration, acetonitrile was diluted in ethanol, while isopropanol was diluted in cyclohexane, which is transparent within the working wavelength range.

To highlight the detection of acetonitrile in ethanol through spectral analysis, the transmission spectra of the ChGs sensor were recorded at various volume concentrations, ranging from 5% to 70%. The interaction length between the guided light and the solution was set at 7.8 mm using sample A. The transmission curves as a function of wavelength for different concentrations are shown in Fig. 5(c). For each point, the acquisition was averaged over three measurements, each lasting 300 ms at any given wavelength. Normalization of the curves was performed by dividing each transmission signal by that of the pure Ethanol. There is a strong correlation between the database spectra and our experimental measurements. A significant decrease in transmission is clearly observed at the wavelength corresponding to the absorption peak associated with the C≡N stretching vibration at $\lambda = 4.44$ µm. A secondary absorption peak at $\lambda = 4.36$ µm is also detected.

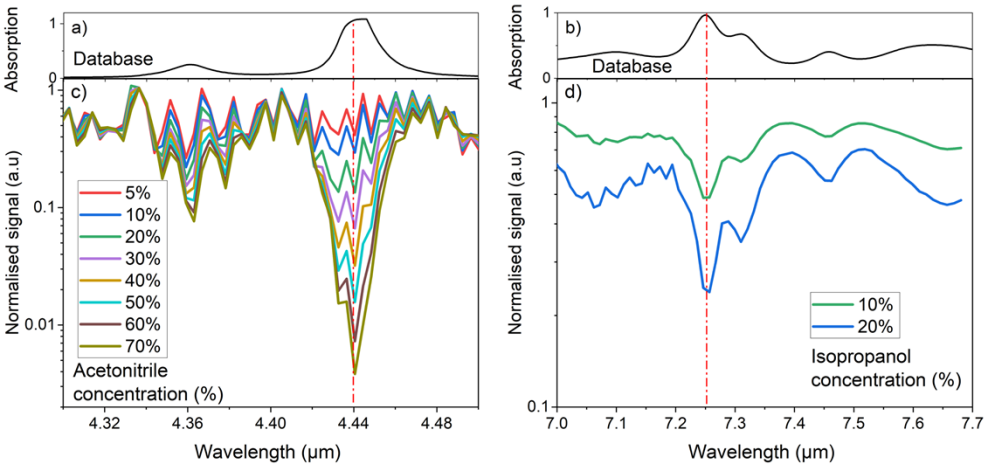

Fig. 5. Normalized absorption spectra from Ref. [61] for a) acetonitrile and b) isopropanol; Normalized ChGs waveguide transmission spectra for sensing of c) acetonitrile and d) isopropanol

Optics EXPRESS

Two solutions of isopropanol in cyclohexane were also prepared with 10% and 20% concentrations. These measurements, shown in Fig. 5(d), were taken using Sample B, with an interaction length of 5.8 mm. A spectral signature similar to that found in the Ref. [61] for isopropanol in this wavelength range was observed. The ν(C-C) stretching vibrational mode at λ = 7.25 µm is distinctly observed.

To better visualize the sensor response as a function of analyte concentration, wavelength emission was tuned to the maximum absorption peaks at 4.44 µm for acetonitrile and 7.25 µm for isopropanol. The acquisition was averaged more than 15 seconds for each concentration. These data are then plotted as a function of their respective concentrations in Fig. 6 for acetonitrile and isopropanol. The curves show good agreement with the decreasing exponential fit of the Beer-Lambert law:

$$P = P_0\, e^{-(\,\epsilon\, \Gamma L\, C\,)} \tag{4}$$

With P_0 being the input optical power, ε the molar absorption coefficient of the analyte, Γ the external confinement factor, C the concentration, and L the interaction length.

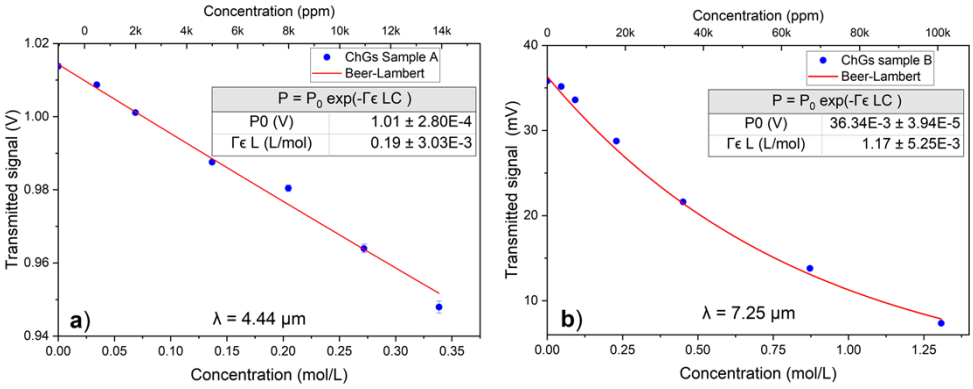

Fig. 6. Transmitted signal amplitude as a function of a) acetonitrile concentration diluted in ethanol for a fixed wavelength at λ = 4.44 µm with an interaction length L = 7.8 mm b) isopropanol concentration diluted in cyclohexane for a fixed wavelength at λ = 7.25 µm with an interaction length L = 5.8 mm.

The sensitivity S at the origin of each curve in Fig. 6 was firstly estimated to calculate the Limit of Detection (LoD). From Eq. (4), the sensitivity can be calculated by differentiating the signal P with respect to the concentration C:

$$S = \frac{dP}{dC} = \epsilon\, \Gamma L\, P_{C=0} \tag{5}$$

The LoD can then be calculated using the following equation [66]:

$$LoD = 3.3\, \frac{\sigma}{S} \tag{6}$$

where σ is the standard deviation of the system noise.

From the data and of Fig. 6(a), we determined that the standard deviation of the signal at C = 0 mol.L^{-1} was 0.68 mV. Additionally, the sensitivity of the measurement was calculated to be 96.2 nW L.mol^{-1}. Using these values, we estimated the LoD for acetonitrile sensing at 610 ppm (11.7 mmol.L^{-1}) at λ = 4.44 µm. Regarding Fig. 6(b), With a standard deviation of the signal at C = 0 mol.L^{-1} of 48.3 µV and a sensitivity of 1.55 nW L.mol^{-1}, a LoD of 300 ppm (3.8 mmol.L^{-1}) was determined for isopropanol at λ = 7.25 µm. We note that the reduced standard deviation

Optics EXPRESS

observed in isopropanol sensing at 7.25 µm is directly attributed to the performance of the liquid nitrogen-cooled *DSS-MCT(14)-020 L* detector, which minimizes thermal noise. This detector differs from the thermoelectrically cooled *DSS-PSE020 T* used for acetonitrile sensing.

The performance of integrated optical sensors is generally evaluated by comparing their LoD values. However, this approach can compromise the fairness of the evaluation, particularly in terms of transduction, as it introduces biases related to the stability and resolution of both the laser source and the detector. A specific criterion focuses exclusively on the transducer part of the sensor, namely the figure of merit (FoM), which depends on two parameters of the transducer: the propagation losses α and the external confinement factor Γ:

$$FOM = \frac{\Gamma}{\alpha} \tag{7}$$

The FoM (in cm) demonstrates that minimizing propagation losses and maximizing the external confinement factor enhances the transducer's performance, independently of the laser source and detector.

Table 2 compares the sensing characteristics of the ChGs platform with other works. It has been reported in the literature that IPA detection in acetone at a concentration of 5% was achieved using a germanium waveguide deposited on SiN at $\lambda = 3.73$ µm, with propagation losses of 7.86 dB/cm [67]. However, the high concentration in this reference can be explained by the weak absorption of isopropanol at $\lambda = 3.73$ µm compared to $\lambda = 7.25$ µm, even though the FoM achieved for this transducer is the highest in Table 2, nother study reported a diamond waveguide with losses of 5 dB/cm at $\lambda = 7.215$ µm, used for isopropanol detection with a LoD of 650 ppm [68].

Table 2. Comparison of sensing performance of the ChGs platform with literature for liquid phase molecule detection

Molecules	λ (µm)	Structure	Interaction length (cm)	Losses (dB/cm)	Γ (%)	LoD (ppm)	FoM (cm)	Ref
IPA	3.73	ChGs	0.402	7.86	12.8	50000	0.07	[67]
IPA	7.215	Diamond	0.5	5	-	650	-	[68]
IPA	7.25	ChGs	0.58	7.7	1.4 - 9.1	300	0.01–0.03	This work
Toluene	6.68	GOS	0.16	5	1.1	7	0.01	[5]
NH_3	9.54	GOS	0.052	1	1.2	0.4	0.05	[69]
Acetonitrile	4.44	ChGs	0.78	11	1.4 - 9.1	610	0.01–0.04	This work

Other studies have reported results on different liquids, such as toluene, which was detected at $\lambda = 6.68$ µm with an LoD of 7 ppm using a germanium waveguide on silicon with propagation losses of 5 dB/cm [5]. The low associated FoM suggests that this performance was achieved due to the stability of the laser source and detector used. A similar GOS platform with losses of 1 dB/cm was used for ammonia detection with an LoD of 0.4 ppm at $\lambda = 9.54$ µm [69]. The FoM calculated in [5] and [69] is closer to that of our transducer used for acetonitrile detection, with which we obtained an LoD of 610 ppm. We suppose that with the same stability of the laser and detector as in [5] and [69], our LoD for acetonitrile detection could be much lower.

3.2. Gas sensing tests

For CO_2 sensing, different concentrations were prepared by diluting CO_2 with nitrogen using flexible pipes that mix gas from two cylinders containing 100% N_2 and CO_2. The flow rates of the gases are regulated using a flow rate controller, with N_2 at 100 sccm (*standard cubic centimeters per minute*) and CO_2 at 50 sccm. The transmission spectra were measured for the two different

Optics EXPRESS

platforms, using ChGs sample A, and PSi sample C. The interaction lengths between the guided light and CO_2 were 10.8 mm and 8.3 mm, respectively. The maximum recorded absorption peaks correspond to the two absorption peaks listed at 4.23 μm and 4.28 μm in the *HITRAN* database [70], as shown in Fig. 7(a) and Fig.7b. For the ChGs sample, transmission spectra were recorded for a CO_2 concentration of 35%, as presented in Fig. 7(c).

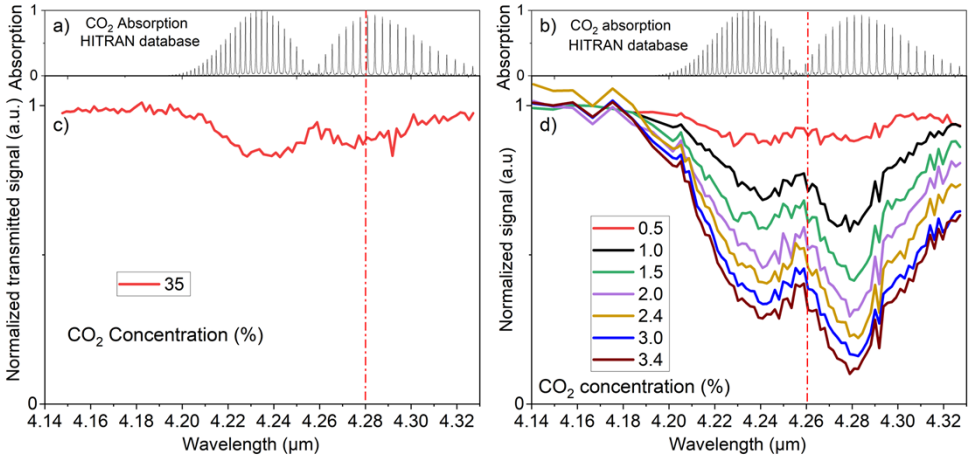

Fig. 7. a),b) Normalized CO_2 Absorption from 4.14 to 4.33 μm from HITRAN database [70]. Normalized transmission spectra for sensing of CO_2 c) using ChGs waveguide and d) using PSi waveguide.

For the PSi sample, Fig. 7(d) shows transmission spectra for seven CO_2 concentrations ranging from 0.5% to 3.4%. A signal drop, corresponding to CO_2 absorption is observed starting at 0.5% concentration for the PSi platform. For the ChGs platform, the concentration needs to be increased to 35% to reach a comparable absorption level, using only about 20% of the detector's dynamic range. By contrast, measurements with the PSi platform show that a CO_2 concentration of just 3.4% can cover nearly the full dynamic range, demonstrating a significantly higher sensitivity compared to the ChGs platform.

In a similar approach to liquid sensing, we performed fixed wavelength measurements around the CO_2 absorption peaks. For the ChGs platform, the emission was tuned to the peak at 4.28 μm. As the signal drops quickly to the detector's noise floor at 4.28 μm or the PSi platform, we shifted the emission wavelength to 4.26 μm, and a shorter waveguide of 5.8 mm was used for fixed wavelength measurements.

Sensing experiments with the PSi platform in Fig. 8(b) show a significantly higher Beer-Lambert exponential coefficient than that with the ChGs platform (Fig. 8(a)). Taking into account the difference in absorption values at 4.28 μm and 4.26 μm, which results in a ratio of 1.86 (Fig. 7(d)), along with the difference in waveguide lengths, 0.78 cm for ChGs and 0.58 cm for PSi, the external confinement factor for PSi is 75 times greater than that of the ChGs platform. This ratio is closer to the *FIMMWAVE* simulated value of Γ for the TM mode, as summarized in Table 1.

From data of Fig. 8, a LoD of 17300 ppm at $\lambda = 4.28$ μm was estimated for the CO_2 sensing using ChGs platform. Regarding PSi platform, the estimated LoD was of 600 ppm at $\lambda = 4.26$ μm.

Table 3 compares the performance of the two CO_2 sensors developed in this work with those from the literature. In Ref. [71], a LoD of 500 ppm was reported, which is better than the 1000 ppm in [72]. However, this reference reported a higher Γ and lower propagation losses. This difference may be explained by the stability of the laser and detector used during the

Optics EXPRESS

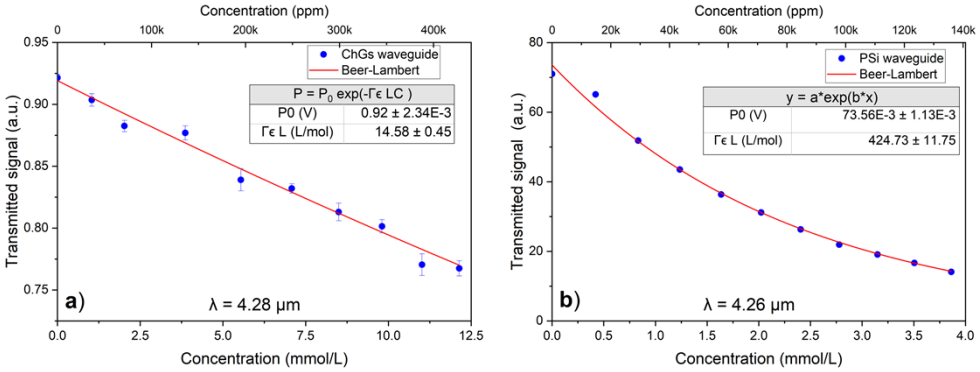

Fig. 8. Transmitted signal amplitude as a function of CO_2 concentration using a) ChGs platform at λ = 4.28 μm with an interaction length L = 7.8 mm b) PSi platform at λ = 4.26 μm with an interaction length L = 5.8 mm.

measurements in [71]. Additionally, the acquisition time was likely optimized to achieve such a LoD without resorting to WMS (*wavelength modulation spectroscopy*). The comparison criterion, which considers the transduction part of the sensor to be the FoM, highlights the performance of the suspended silicon sensor from [72] as superior to that of [71]. For our ChGs sensor, we achieved a FoM closer to that reported in Ref. [21], which is attributed to the low external confinement factor, amounting to only a few percent. Regarding the PSi sensor, its external confinement factor is the highest among the studies compared here, due to its enhanced bulk interaction. However, when comparing the FoM, its high loss values place it behind Ref. [72]. The losses in the PSi platform are high relative to other references, approaching those of the Si slot sensor mentioned in [55], which was used for CH_4 detection and achieved a LoD of only 1.54 ppm despite losses of 8.3 dB/cm. This demonstrates the effectiveness of bulk detection. In Ref. [55], the authors initially had 14 dB/cm losses but managed to reduce this to 8 dB/cm by performing an annealing process at 115°C while keeping the sample under nitrogen during measurement. The high losses observed in platforms with bulk interaction are mainly due to the adsorption of various molecules present in the ambient air within the guiding structures.

Table 3. Comparison of the characteristics of developed ChGs and PSi sensors with literature sensors for CO_2 detection

Molecules	λ (μm)	Structure	Interaction length (cm)	Losses (dB/cm)	Γ (%)	LoD (ppm)	FoM (cm)	Ref
CO_2	4.319	ChGs	1	5.1	4.6	25000	0.04	[21]
CO_2	4.26	Si ridge	2	3.98	14 - 16	500	0.15 - 0.17	[71]
CO_2	4.24	Si suspend	0.32	3	44	1000	0.64	[72]
CH_4	3.27	Si slot	1.15	8.3	69	1.54	0.36	[55]
CO_2	4.28	ChGs	1.08	6.8	1.4–9.1	17300	0.01 - 0.06	This work
CO_2	4.26	PSi	0.58	11.4	111 - 115	600	0.42–0.44	This work

In the case of porous silicon, free-carrier absorption in the highly doped silicon substrate and bulk scattering also increases propagation losses. Additionally, silicon oxide forms on the sample surface due to interaction with the ambient air. Despite these high losses, the FoM of the PSi platform remains significantly well placed compared to other sensors. We estimate that the

Optics EXPRESS

performance of the PSi sensor could be further improved by using the optimal calculated length of 4 mm, which is approximately equal to the inverse of the propagation losses.

3.3. Complex medium

Sensing in a complex environment within integrated optics presents a challenge, with few initiatives identified to our knowledge. As a proof of concept and to validate our sensor, we explored the deconvolution of spectra from mixtures of two distinct solutions. We began by preparing two stocks solutions by diluting 1-propanol and 2-propanol in acetonitrile with a concentration of 20%. Then, using these solutions, we prepared five mixtures with varying concentrations. Based on the spectra of these five mixtures and applying standard numerical processing using the least-squares method, we were able to approximate the concentrations of the two components (1-propanol and 2-propanol) within a mixture by leveraging the spectral fingerprints of the original solutions. Figure 9 shows the measurement obtained from a test solution prepared by mixing the two stock solutions, with a ratio of 50%.

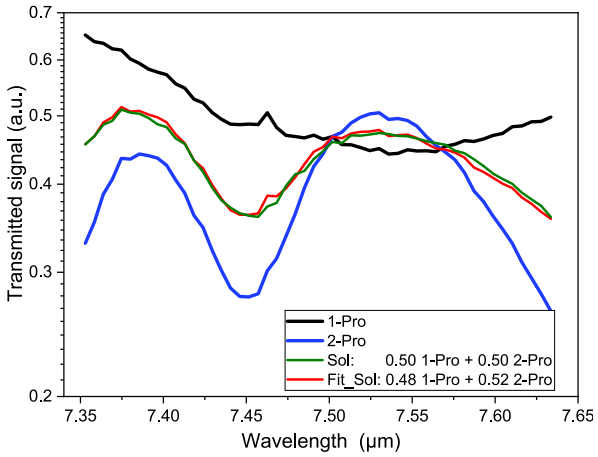

Fig. 9. Normalized transmission of the ChGs waveguide as a function of wavelength with three different solutions in the fluidic cell: 1-propanol, 2-propanol and a mixed solution with 50% ratio of 1-propanol and 2-propanol.

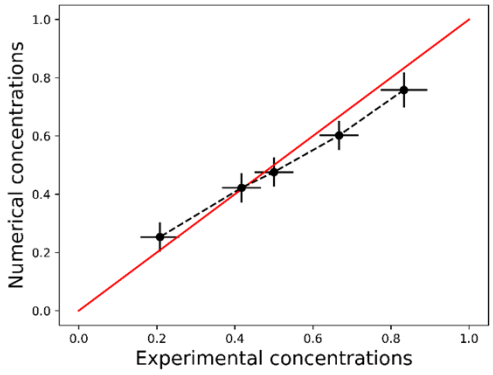

Fig. 10. Evaluation of correspondence between experimental and numerical concentrations.

Optics EXPRESS

The developed numerical program aims to identify factors α and β such that the absorption of the combination of the two stock solutions, when scaled by these factors, closely matches the absorption of the mixed solution. This is achieved by minimizing the following function:

$$Fonction\ \left(Abs_{mix}, Abs_{\ 1pro}, Abs_{\ 2pro}\right) = Abs_{mix} - \left(\alpha \quad Abs_{\ 1pro} \ + \ \beta \ \ Abs_{\ 2pro}\right) \tag{8}$$

Where Abs_{mix} represents the absorption of the mixed solution, and Abs_{1pro} et Abs_{2pro} are the absorptions of the stock solutions containing 20% 1-propanol and 20% 2-propanol in acetonitrile, respectively.

Table 4 summarizes both the experimental concentrations and those estimated by the numerical model for each prepared solution. These data are presented in Fig. 10. The results indicate a trend where the numerically estimated concentrations align with the experimental concentrations, even with a standard adjustment based on the least squares method. However, it is worth noting that a more sophisticated numerical treatment could further refine the results. These findings highlight promising prospects for the compatibility of evanescent wave-based optical transduction in complex environments.

Table 4. Comparison between the experimental concentrations of the solutions and those estimated by deconvolution model. The uncertainties in the calculated concentrations are based on a reading error of 0.05 ml, with solution volumes of 1.5 ml for solutions 1 and 2 ml for the other solutions

	Prepared concentrations		Model estimation	
Solutions	**1-Propanol (20%)**	**2-Propanol (20%)**	**1-Propanol (20%)**	**2-Propanol (20%)**
Solution 1	0.833 ± 0.066	0.167 ± 0.066	0.758 ± 0.066	0.242 ± 0.066
Solution 2	0.667 ± 0.050	0.333 ± 0.050	0.602 ± 0.050	0.397 ± 0.050
Solution 3	0.500 ± 0.050	0.500 ± 0.050	0.476 ± 0.050	0.524 ± 0.050
Solution 4	0.417 ± 0.050	0.583 ± 0.050	0.422 ± 0.050	0.578 ± 0.050
Solution 5	0.208 ± 0.050	0.792 ± 0.050	0.253 ± 0.050	0.747 ± 0.050

4. Conclusion

This work evaluated the performance of the two platforms, ChGs and PSi, in terms of integrated optics sensing in the mid-IR range. The ChGs waveguides exhibit a wide transparency range from λ = 3.94 to 8.95 μm, with a minimum propagation losses value of 2.5 dB/cm at λ = 7.58 μm, while PSi transparency range was from λ = 3.94 to 4.55 μm with a minimum propagation losses value of 9.1 dB/cm at λ = 4.12 μm.

Sensing measurements were conducted using Carbon dioxide to demonstrate gas phase transduction, while acetonitrile and isopropanol were used for the liquid phase. These measurements were carried out either through wavelength scans to observe the evolution of absorption spectra based on the concentration of the targeted molecules or statically by fixing the wavelength corresponding to an absorption peak of the analyte. The results showed an estimated LoD of 610 ppm at λ = 4.44 μm for acetonitrile and 300 ppm at λ = 7.25 μm for isopropanol, enabled by the evanescent field interaction. Regarding gas sensing, CO_2 was detected with a LoD of 17000 ppm at λ = 4.28 μm using ChGs platform. The sensing application was improved with PSi platform. Enhancement of the external confinement factor was experimentally observed during CO_2 sensing, exceeding 75 times ChGs platform. Due to the open pores, light and gas molecules interact within the internal volume, unlike ChGs platform where the interaction occurs with the evanescent part of the light. This volume interaction leads to a LoD of 600 ppm at λ = 4.26 μm for CO_2 sensing. To introduce sensing in complex environment, the extraction of concentrations from mixtures of two solutions was performed through deconvolution of

Optics EXPRESS

the measured spectra, yielding good approximations. These results validate the transduction capabilities of the developed platforms in complex environments. Further expertise in signal processing could enhance the analysis and improve transduction performance in the environment with multiple analytes.

Funding. HORIZON EUROPE Framework Programme (101092723, IBAIA); Agence Nationale de la Recherche (ANR-21-CE04-011, AQUAE); Région Bretagne; Lannion-Trégor Communauté.

Acknowledgments. The ChGs layers fabrication was performed Thanks to Institut des Sciences Chimiques de Rennes (ISCR) and the technological processing of ridge waveguides was performed in the Centre Commun Lannionnais d'Optique (CCLO)-technological platforms which is supported by the French RENATECH + network.

Disclosures. The authors declare no conflicts of interest.

Data availability. Data underlying the results presented in this paper are not publicly available but may be obtained from the authors upon reasonable request.

References

1. V. Mittal, G. Z. Mashanovich, and J. S. Wilkinson, "Perspective on thin film waveguides for on-chip mid-infrared spectroscopy of liquid biochemical analytes," Anal. Chem. **92**(16), 10891–10901 (2020).
2. F. Cheng, J. Zhang, Y. Guan, *et al.*, "Ultralow power consumption of a quantum cascade laser operating in continuous-wave mode at room temperature," Opt. Express **28**(24), 36497–36504 (2020).
3. R. Q. Yang, L. Li, W. Huang, *et al.*, "InAs-based interband cascade lasers," IEEE J. Sel. Top. Quantum Electron. **25**(6), 1–8 (2019).
4. M. Montesinos Ballester, C. Lafforgue, A. Ballabio, *et al.*, "On-chip mid-infrared supercontinuum generation from 3 to 13 µm wavelength," ACS Photonics **7**(12), 3423–3429 (2020).
5. N. Teigell Benéitez, B. Baumgartner, J. Missinne, *et al.*, "Mid-IR sensing platform for trace analysis in aqueous solutions based on a germanium-on-silicon waveguide chip with mesoporous silica coating for analyte enrichment," Opt. Express **28**(18), 27013–27027 (2020).
6. B. J. Eggleton, "Chalcogenide photonics: fabrication, devices and applications Introduction," Opt. Express **18**(25), 26632–26634 (2010).
7. B. J. Eggleton, B. Luther-Davies, and K. Richardson, "Chalcogenide photonics," Nat. Photonics **5**(3), 141–148 (2011).
8. L. Petit, N. Carlie, B. Zdyrko, *et al.*, "Progress on the fabrication of on-chip, integrated chalcogenide glass (ChG)-based sensors," in *Frontiers in Optics 2009/Laser Science XXV/Fall 2009 OSA Optics & Photonics Technical Digest (2009), Paper AWB2* (Optica Publishing Group, 2009), p. AWB2.
9. E. Baudet, A. Gutierrez-Arroyo, P. Němec, *et al.*, "Selenide sputtered films development for MIR environmental sensor," Opt. Mater. Express **6**(8), 2616 (2016).
10. J. Lucas, J. Troles, X. H. Zhang, *et al.*, "Glasses to see beyond visible," C. R. Chim. **21**(10), 916–922 (2018).
11. M. D. Pelusi, V. G. Ta'eed, Libin Fu, *et al.*, "Applications of highly-nonlinear chalcogenide glass devices tailored for high-speed all-optical signal processing," IEEE J. Select. Topics Quantum Electron. **14**(3), 529–539 (2008).
12. V. G. Ta'eed, N. J. Baker, L. Fu, *et al.*, "Ultrafast all-optical chalcogenide glass photonic circuits," Opt. Express **15**(15), 9205–9221 (2007).
13. L. Bodiou, M. Baillieul, V. Nazabal, *et al.*, "Carbon dioxide mid-infrared sensing based on Dy^{3+}-doped chalcogenide waveguide photoluminescence," Opt. Lett. **48**(5), 1128–1131 (2023).
14. R. Sharma, S. Kaur, P. Chauhan, *et al.*, "Computational design & analysis of GeSe2-As2Se3-PbSe based rib waveguide for mid-infrared supercontinuum generation," Optik **220**, 165032 (2020).
15. V. Mittal, N. P. Sessions, J. S. Wilkinson, *et al.*, "Optical quality ZnSe films and low loss waveguides on Si substrates for mid-infrared applications," Opt. Mater. Express **7**(3), 712–725 (2017).
16. P. Ma, D.-Y. Choi, Y. Yu, *et al.*, "High Q factor chalcogenide ring resonators for cavity-enhanced MIR spectroscopic sensing," Opt. Express **23**(15), 19969 (2015).
17. P. Ma, D.-Y. Choi, Y. Yu, *et al.*, "Low-loss chalcogenide waveguides for chemical sensing in the mid-infrared," Opt. Express **21**(24), 29927–29937 (2013).
18. M. Pi, C. Zheng, J. Ji, *et al.*, "Mid-infrared chalcogenide waveguide ch4 sensor based on surface-enhanced infrared absorption spectroscopy," in *2022 Photonics & Electromagnetics Research Symposium (PIERS)* (2022), pp. 214–218.
19. V. Mittal, M. Nedeljkovic, D. J. Rowe, *et al.*, "Chalcogenide glass waveguides with paper-based fluidics for mid-infrared absorption spectroscopy," Opt. Lett. **43**(12), 2913–2916 (2018).
20. L. Qiao, Z. Zheng, and W. Sun, "A study on SF6 gas sensor on MEMS," in *2020 IEEE International Conference on Artificial Intelligence and Computer Applications (ICAICA)* (2020), pp. 1087–1090.
21. M. Pi, C. Zheng, H. Zhao, *et al.*, "Mid-infrared ChG-on-MgF_2 waveguide gas sensor based on wavelength modulation spectroscopy," Opt. Lett. **46**(19), 4797 (2021).
22. H. F. Arrand, T. M. Benson, P. Sewell, *et al.*, "The application of porous silicon to optical waveguiding technology," IEEE J. Sel. Top. Quantum Electron. **4**(6), 975–982 (1998).

Optics EXPRESS

23. P. Girault, P. Azuelos, N. Lorrain, *et al.*, "Porous silicon micro-resonator implemented by standard photolithography process for sensing application," Opt. Mater. **72**, 596–601 (2017).
24. L. Moretti, I. Rea, L. De Stefano, *et al.*, "Periodic versus aperiodic: Enhancing the sensitivity of porous silicon based optical sensors," Appl. Phys. Lett. **90**(19), 191112 (2007).
25. F. S. H. Krismastuti, S. Pace, and N. H. Voelcker, "Porous silicon resonant microcavity biosensor for matrix metalloproteinase detection," Adv. Funct. Mater. **24**(23), 3639–3650 (2014).
26. G. Barillaro, P. Bruschi, F. Pieri, *et al.*, "CMOS-compatible fabrication of porous silicon gas sensors and their readout electronics on the same chip," Phys. Status Solidi A **204**(5), 1423–1428 (2007).
27. G. Z. Mashanovich, M. M. Milošević, M. Nedeljkovic, *et al.*, "Low loss silicon waveguides for the mid-infrared," Opt. Express **19**(8), 7112 (2011).
28. M. Duris, M. Guendouz, N. Lorrain, *et al.*, "Vertical multilayer structures based on porous silicon layers for mid-infrared applications," Opt. Mater. Express **10**(8), 1921–1930 (2020).
29. L. Canham, ed., *Handbook of Porous Silicon* (Springer International Publishing, 2018).
30. S. Meziani, A. Jaafar, A. Hammouti, *et al.*, "Volume detection based on porous silicon waveguide for CO_2 mid-infrared spectroscopy," Opt. Express **32**(8), 13628 (2024).
31. A. Loni, "Porous silicon formation by anodization," in *Handbook of Porous Silicon*, L. Canham, ed. (Springer International Publishing, 2014), pp. 11–22.
32. T. E. Bell, P. T. J. Gennissen, D. DeMunter, *et al.*, "Porous silicon as a sacrificial material," J. Micromech. Microeng. **6**(4), 361–369 (1996).
33. C.-S. Lee, J.-D. Lee, and C.-H. Han, "A new wide-dimensional freestanding microstructure fabrication technology using laterally formed porous silicon as a sacrificial layer," Sens. Actuators, A **84**(1-2), 181–185 (2000).
34. S. W. Leonard, J. P. Mondia, H. M. van Driel, *et al.*, "Tunable two-dimensional photonic crystals using liquid crystal infiltration," Phys. Rev. B **61**(4), R2389–R2392 (2000).
35. A. Bobrovsky, S. Svyakhovskiy, A. Bogdanov, *et al.*, "Photocontrollable photonic crystals based on porous silicon filled with photochromic liquid crystalline mixture," Adv. Opt. Mater. **8**(22), 2001267 (2020).
36. B. King and M. J. Sailor, "Medium-wavelength infrared gas sensing with electrochemically fabricated porous silicon optical rugate filters," J. Nanophoton **5**(1), 051510 (2011).
37. Y. Qin, Y. Liu, and Y. Wang, "Aligned array of porous silicon nanowires for gas-sensing application," ECS J. Solid State Sci. Technol. **5**(7), P380–P383 (2016).
38. F. A. Harraz, A. A. Ismail, H. Bouzid, *et al.*, "Electrical porous silicon sensor for detection of various organic molecules in liquid phase," Phys. Status Solidi A **212**(8), 1851–1857 (2015).
39. A. Foucaran, B. Sorli, M. Garcia, *et al.*, "Porous silicon layer coupled with thermoelectric cooler: a humidity sensor," Sensors and Actuators A: Physical **79**(3), 189–193 (2000).
40. Z. M. Rittersma, A. Splinter, A. Bödecker, *et al.*, "A novel surface-micromachined capacitive porous silicon humidity sensor," Sensors and Actuators B: Chemical **68**(1-3), 210–217 (2000).
41. S.-J. Kim, B.-H. Jeon, and K.-S. Choi, "Improvement of the sensitivity by UV light in alcohol sensors using porous silicon layer," in *CAS '99 Proceedings. 1999 International Semiconductor Conference (Cat. No.99TH8389)* (1999), 2, pp. 475–478 vol.2.
42. S. Chan, P. M. Fauchet, Y. Li, *et al.*, "Porous silicon microcavities for biosensing applications," phys. stat. sol. (a) **182**(1), 541–546 (2000).
43. L. De Stefano, P. Arcari, A. Lamberti, *et al.*, "DNA optical detection based on porous silicon technology: from biosensors to biochips," Sensors **7**(2), 214–221 (2007).
44. G. Rong, A. Najmaie, J. E. Sipe, *et al.*, "Porous silicon waveguides for DNA detection," in *3rd IEEE International Conference on Group IV Photonics, 2006.* (2006), pp. 13–15.
45. T. Laurell, J. Drott, M. Bengtsson, *et al.*, "Optimisation of porous silicon used as a glucose biosensor enzyme carrier matrix," in *Proceedings of the 20th Annual International Conference of the IEEE Engineering in Medicine and Biology Society. Vol.20 Biomedical Engineering Towards the Year 2000 and Beyond (Cat. No.98CH36286)* (1998), 6, pp. 2876–2878 vol.6.
46. S. E. Létant, B. R. Hart, S. R. Kane, *et al.*, "Enzyme immobilization on porous silicon surfaces," Adv. Mater. **16**(8), 689–693 (2004).
47. L. De Stefano, L. Moretti, I. Rendina, *et al.*, "Porous silicon microcavities for optical hydrocarbons detection," Sensors and Actuators A: Physical **104**(2), 179–182 (2003).
48. E. V. Osipov, I. L. Martynov, D. S. Dovzhenko, *et al.*, "Fabrication of optical sensors based on porous silicon microcavities with embedded conjugated polymers for explosives detection," in *2018 International Conference Laser Optics (ICLO)* (2018), pp. 389.
49. J. T. Robinson, K. Preston, O. Painter, *et al.*, "First-principle derivation of gain in high-index-contrast waveguides," Opt. Express **16**(21), 16659–16669 (2008).
50. A. Jaafar, S. Meziani, A. Hammouti, *et al.*, "Oxidation effect on optical properties of integrated waveguides based on porous silicon layers at mid-infrared wavelength," Photonics and Nanostructures - Fundamentals and Applications **58**, 101244 (2024).
51. J. E. Spanier and I. P. Herman, "Use of hybrid phenomenological and statistical effective-medium theories of dielectric functions to model the infrared reflectance of porous SiC films," Phys. Rev. B **61**(15), 10437–10450 (2000).

Optics EXPRESS

52. X. Wang, K. Jiao, G. Farrell, *et al.*, "Chalcogenide glass preparation, purification and fiber fabrication," in *Mid-Infrared Fluoride and Chalcogenide Glasses and Fibers*, P. Wang, X. Wang, and H. Guo, et al., eds. (Springer Nature, 2022), pp. 99–171.
53. D. K. Schroder, R. N. Thomas, and J. C. Swartz, "Free carrier absorption in silicon," IEEE Trans. Electron Devices **25**(2), 254–261 (1978).
54. P. Ferrand and R. Romestain, "Optical losses in porous silicon waveguides in the near-infrared: Effects of scattering," Appl. Phys. Lett. **77**(22), 3535–3537 (2000).
55. H. D. Yallew, M. Vlk, A. Datta, *et al.*, "Sub-ppm methane detection with mid-infrared slot waveguides," ACS Photonics **10**(12), 4282–4289 (2023).
56. J. S. Penadés, A. Sánchez-Postigo, M. Nedeljkovic, *et al.*, "Suspended silicon waveguides for long-wave infrared wavelengths," Opt. Lett. **43**(4), 795–798 (2018).
57. K. Gallacher, R. W. Millar, U. Griškevičiūte, *et al.*, "Low loss Ge-on-Si waveguides operating in the 8-14 Mm atmospheric transmission window," Opt. Express **26**(20), 25667–25675 (2018).
58. M. Brun, P. Labeye, G. Grand, *et al.*, "Low loss SiGe graded index waveguides for mid-IR applications," Opt. Express **22**(1), 508 (2014).
59. A. Gutierrez-Arroyo, E. Baudet, L. Bodiou, *et al.*, "Optical characterization at 7.7 μm of an integrated platform based on chalcogenide waveguides for sensing applications in the mid-infrared," Opt. Express **24**(20), 23109 (2016).
60. P. Ma, D.-Y. Choi, Y. Yu, *et al.*, "Low-loss chalcogenide waveguides for biosensing in the mid-infrared," in *2014 IEEE Photonics Society Summer Topical Meeting Series* (2014), pp. 59–60.
61. T. L. Myers, R. G. Tonkyn, T. O. Danby, *et al.*, "Accurate measurement of the optical constants n and k for a series of 57 inorganic and organic liquids for optical modeling and detection," Appl Spectrosc **72**(4), 535–550 (2018).
62. B. Smith, "Organic nitrogen compounds IV: nitriles," **34**, 18–21, 44 (2019).
63. P. H. Reinsberg and H. Baltruschat, "Potential- and cation-dependent adsorption of acetonitrile on gold investigated via surface enhanced infrared absorption spectroscopy," Electrochim. Acta **334**, 135609 (2020).
64. G. A. Carvalho and S. Pilling, "Chemical changes induced during heating of acetonitrile-rich ice pre-irradiated by X-rays and its implication in astrochemistry," Spectrochim. Acta, Part A **267**, 120495 (2022).
65. F. Waidhas, S. Haschke, P. Khanipour, *et al.*, "Secondary alcohols as rechargeable electrofuels: electrooxidation of isopropyl alcohol at Pt electrodes," ACS Catal. **10**(12), 6831–6842 (2020).
66. B. W. Pack, S. Stithit, and W. Chen, "Clinical supplies manufacture," in *Developing Solid Oral Dosage Forms* (Elsevier, 2017), pp. 653–676.
67. W. Li, P. Anantha, K. H. Lee, *et al.*, "Spiral waveguides on germanium-on-silicon nitride platform for mid-IR sensing applications," IEEE Photonics J. **10**(3), 1–7 (2018).
68. P. Forsberg, P. Hollman, and M. Karlsson, "High sensitivity infrared spectroscopy with a diamond waveguide on aluminium nitride," Analyst **146**(22), 6981–6989 (2021).
69. U. Griskeviciute, U. Griskeviciute, R. W. Millar, *et al.*, "Ge-on-Si waveguides for sensing in the molecular fingerprint regime," Opt. Express **28**(4), 5749–5757 (2020).
70. I. E. Gordon, L. S. Rothman, C. Hill, *et al.*, "The HITRAN2016 molecular spectroscopic database," J. Quant. Spectrosc. Radiat. Transfer **203**, 3–69 (2017).
71. C. Ranacher, C. Consani, N. Vollert, *et al.*, "Characterization of evanescent field gas sensor structures based on silicon photonics," IEEE Photonics J. **10**(5), 1–14 (2018).
72. F. Ottonello-Briano, C. Errando-Herranz, H. Rödjegård, *et al.*, "Carbon dioxide absorption spectroscopy with a mid-infrared silicon photonic waveguide," Opt. Lett. **45**(1), 109–112 (2020).